https://doi.org/10.5194/egusphere-2026-3498
Preprint. Discussion started: 21 July 2026

A Hierarchical Fractional N-body Framework for Coulomb Stress Evolution in Fault Networks: Exact Analytical Solutions and Falsifiable Seismicity Scaling Laws

Farrukh A. Chishtie[1,2,3]

[1]Peaceful Society, Science and Innovation Foundation, Vancouver, BC, Canada

[2]Faculty of Land and Food Systems, University of British Columbia, Vancouver, BC, Canada

[3]Department of Occupational Science and Occupational Therapy, University of British Columbia, Vancouver, BC, Canada

Correspondence: fachisht@uwo.ca

Abstract

We develop an exact analytical framework for the hierarchical fractional dynamics of interacting many-body systems and apply it to the nonlinear Coulomb stress transfer that governs seismicity in fractally organised fault networks. The framework rests on a scaling relation $\alpha_k = 2 - 2/(N_k + 1)$ that connects the order of a Riemann–Liouville fractional evolution equation at hierarchical level k to the number N_k of interacting bodies at that level, derived in a companion paper (Chishtie, 2026, *Physics Open*)

https://doi.org/10.5194/egusphere-2026-3498
Preprint. Discussion started: 21 July 2026

and applied here to the seismogenic setting. Closed-form solutions are obtained via parametric trigonometric representations $\sigma_k(\theta) \propto \sin^4\theta$ at each level together with Chebyshev polynomial inversions of the time–parameter relation, and they converge to the classical wave equation as $N_k \to \infty$. We embed the framework into the Time-Dependent Stress Response (TDSR) seismicity model of Dahm and Hainzl (2022, *J. Geophys. Res.*) to describe the hierarchical Coulomb stress cascade through a fractally organised fault network. Three quantitative, falsifiable scaling laws follow from the closed-form solutions with no free parameters: an Omori–Utsu aftershock decay exponent $p_k = \alpha_k/2 = 1 - 1/(N_k + 1)$ that stratifies across generations; a spatial Coulomb stress falloff $\ell^{-(1+\alpha_k)}$ that departs measurably from the classical elastic ℓ^{-3} law; and a Gutenberg–Richter b-value $b_k \approx D_f\, N_k/(N_k + 1)$ that accounts for the longstanding discrepancy between the fractal-dimension expectation $b = D_f \approx 1.5$–2 and the commonly observed $b \approx 1$ as a finite-N_k fractional correction. Numerical verification using the Grünwald–Letnikov scheme against the Mittag-Leffler exact series solution of the fractional relaxation equation confirms the analytical results. The standard TDSR model is recovered exactly as $N_k \to \infty$ at all hierarchical levels and is therefore a special case of the present framework. We present illustrative qualitative comparisons with the 2023 Kahramanmaraş doublet and the 2024 Noto Peninsula earthquake; a systematic generation-stratified analysis across many sequences is set out as the primary observational test of the framework.

Keywords: fractional dynamics; hierarchical N-body problem; Riemann–Liouville derivative; nonlinear geophysics; Coulomb stress transfer; anomalous diffusion; Omori–Utsu law; Gutenberg–Richter relation; fault networks; HfTDSR model.

https://doi.org/10.5194/egusphere-2026-3498
Preprint. Discussion started: 21 July 2026

1 Introduction

Probabilistic seismic hazard assessment depends on seismicity models that can forecast earthquake rates as functions of time, location, and magnitude. Over the past three decades, physics-based models have progressively supplanted purely statistical approaches by grounding rate forecasts in the mechanics of stress transfer and fault failure. The two most widely deployed physics-based formulations are the Coulomb Failure (CF) model (King et al., 1994) and the rate-and-state (RS) model of Dieterich (1994) (see also Heimisson and Segall 2018), both of which operate in the Coulomb stress approximation. A recent synthesis by Dahm and Hainzl (2022) demonstrates that both models are special cases of a broader Time-Dependent Stress Response (TDSR) framework in which earthquake triggering is characterised by a mean time-to-failure

$$\bar{t}_f(\zeta) = t_0 \exp\left(\frac{\zeta}{\delta\sigma}\right), \tag{1}$$

where $\zeta = S_0 - \sigma_c$ is the distance to the Coulomb failure threshold and $\delta\sigma$ is a skin parameter. The total seismicity rate is

$$R(t) = \int_{-\infty}^{\infty} \frac{\chi(\zeta, t)}{\bar{t}_f(\zeta)}\, d\zeta, \tag{2}$$

where $\chi(\zeta, t)$ is the time-evolving density of fault sources at stress level ζ. The TDSR model reproduces Omori–Utsu decay, stress-shadow quiescence, and stationary background seismicity within a single concise formulation.

A fundamental limitation shared by all three models is that the source distribution $\chi(\zeta, t)$ is specified by an effective-medium assumption: every fault element in volume V receives the same Coulomb stress increment and inter-element interactions are absorbed into bulk moduli. This provides no analytical description of the hierarchical stress cascade governing multi-generation aftershock sequences. Natural fault systems are organised hierarchically across many orders of magnitude in scale: tectonic plate boundaries subdivide into major fault zones, which subdivide into individual fault segments, which are resolved further into asperity patches and micro-crack networks. The fractal self-similarity of this struc-

https://doi.org/10.5194/egusphere-2026-3498
Preprint. Discussion started: 21 July 2026

ture is well-documented (Turcotte, 1997; Kagan, 2010), yet neither ETAS (Ogata, 1988) nor TDSR provides an exact, closed-form description of how Coulomb stress evolves level by level through such a hierarchy.

A further modelling limitation concerns the choice of fractional operator. Existing fractional extensions of seismicity models (Michas and Vallianatos, 2023) adopt the Caputo derivative, which restricts the temporal order to unit-bounded intervals and imposes initial conditions in terms of integer-order derivatives. In a seismogenic system with pre-existing deformation history, the physically correct initial conditions involve fractional moments of the stress field, and the order of the governing operator need not be confined to a single unit interval. The Riemann–Liouville (RL) derivative, defined for all $\alpha > 0$, is therefore the more general and physically appropriate choice.

The present paper introduces the Hierarchical Fractional Time-Dependent Stress Response (HfTDSR) framework, which embeds the TDSR formulation within a hierarchical N-body fractional dynamics in which the governing equation at each level carries an RL derivative of order $\alpha_k > 0$. In the companion paper Chishtie (2026), exact analytical solutions to the hierarchical N-body problem were obtained using the scaling relation

$$\alpha_k = 2 - \frac{2}{N_k + 1}, \tag{3}$$

where N_k is the number of bodies (fault segments) at level k. Solutions are expressed in parametric trigonometric form $\sigma(\theta) \propto \sin^4\theta$ and inverted via Chebyshev polynomial expansions, achieving machine-precision accuracy.

We show here that fault segments at level k receiving Coulomb stress from a level-$(k-1)$ rupture constitute precisely such an N_k-body sub-system. The RL fractional order α_k controls the anomalous diffusion of that stress through the surrounding viscoelastic crust, and the parametric solutions provide the exact time evolution of the Coulomb stress increment that enters equation (2). The resulting multi-scale seismicity rate reduces to the TDSR rate of Dahm and Hainzl (2022) exactly in the limit $N_k \to \infty$, confirming that HfTDSR is strictly

https://doi.org/10.5194/egusphere-2026-3498
Preprint. Discussion started: 21 July 2026

more general than TDSR.

The paper is organised as follows. Section 2 establishes the hierarchical fault model and the N-body mapping. Section 3 defines the RL derivative and derives the fractional stress evolution equation with its exact parametric solution. Section 4 integrates these results into the HfTDSR rate formula and derives the three falsifiable scaling laws, each illustrated numerically. Section 5 presents illustrative qualitative comparisons with recent major earthquake sequences. Section 6 discusses implications, limitations, and the systematic observational test required for falsification.

2 The Hierarchical Fault System as an N-body Problem

2.1 Geometry and definitions

We consider a seismogenic volume V cut by a hierarchically organised fault network. At level $k = 0$, a single master fault segment of length L_0 accumulates tectonic strain until it fails in a mainshock. The coseismic stress redistribution perturbs N_1 daughter fault segments at level $k = 1$, each of characteristic length $L_1 < L_0$. Each level-1 segment in turn loads N_2 level-2 sub-segments, and so on to depth K. The characteristic length scale at level k obeys the fractal relation

$$L_k = L_0\,\lambda^k, \qquad \lambda = N^{-1/D_f}, \tag{4}$$

where D_f is the fractal dimension of the fault network ($D_f \approx 1.5$–2.0; Turcotte 1997) and N is the branching ratio, assumed uniform across levels for analytical tractability.

The dominant pairwise interaction between fault segments at level k is elastic. In the asymptotic far-field, the stress transfer kernel between two point dislocations separated by

https://doi.org/10.5194/egusphere-2026-3498
Preprint. Discussion started: 21 July 2026

distance r takes the form (Okada, 1992)

$$K(\mathbf{r}, \mathbf{r}') \sim C\,|\mathbf{r} - \mathbf{r}'|^{-3} \quad \text{as } |\mathbf{r} - \mathbf{r}'| \to \infty. \tag{5}$$

Remark 1 (Scope of equation (5))**.** *Equation* (5) *is the asymptotic far-field elastic Coulomb stress kernel and is used in this paper only to establish the structural identity between the gradient of the elastic inter-segment potential and the gravitational* $1/r^2$ *force of the hierarchical* N*-body system of Chishtie (2026). It is not the spatial Coulomb stress prediction of the HfTDSR model. The HfTDSR spatial prediction is derived in Section 3 as the long-range asymptotic solution of the Riemann–Liouville fractional wave-diffusion equation* (10) *and is given by* $\Delta\sigma_c^{(k)}(\ell) \propto \ell^{-(1+\alpha_k)}$ *(Section 4.3, equation* (16)*). For every finite* $N_k \geq 2$ *this exponent is strictly less than three, so that the HfTDSR Coulomb stress decays more slowly with distance than the classical elastic kernel of equation* (5) *and stress is transferred farther than predicted by purely elastic theory. This anomalous superdiffusion of Coulomb stress is the spatial signature of the underlying fractional dynamics and is the second of the three falsifiable scaling laws developed in Section 4.*

The r^{-3} dependence is structurally identical, at the level of the inter-body force (gradient of the potential), to the gravitational $1/r^2$ force of the N-body problem studied in Chishtie (2026), and this structural identity is the physical foundation of the present mapping.

2.2 The N-body identification

Each fault segment at level k is identified with a body of effective mass $m_k \propto A_k\,\sigma_n$, where σ_n is the effective normal stress and $A_k = L_k^2$ is the segment area. The separation between segments at the same level is $r_k \sim L_{k-1}$. The inter-body potential is the Coulomb stress kernel $K(\mathbf{r}, \mathbf{r}')$, which plays the role of the gravitational potential.

Under these identifications, the hierarchical configuration assumption of Chishtie (2026) maps onto the empirical observation that aftershock clusters are distributed approximately

https://doi.org/10.5194/egusphere-2026-3498
Preprint. Discussion started: 21 July 2026

isotropically around the mainshock epicentre at each hierarchical level (Zaliapin and Ben-Zion, 2013). The exact analytical solutions of Chishtie (2026) then apply directly, with the fractional order at level k given by equation (3) and the inter-body (inter-segment) separation given by the parametric solution

$$\sigma_k(\theta) = \sigma_0^{(k)} \sin^4\theta, \tag{6}$$

where θ is a dimensionless parameter increasing monotonically with physical time and $\sigma_0^{(k)}$ is set by level-k initial conditions.

Proposition 1 (Fractional order hierarchy)**.** *For a seismogenic fault system in which each level-k sub-system consists of N_k equally stressed fault segments interacting via an elastic Coulomb stress kernel of the asymptotic form* (5)*, the order of the governing RL fractional stress evolution equation satisfies $\alpha_k = 2 - 2/(N_k + 1)$, with $\alpha_k \in (1, 2)$ for all $N_k \geq 2$.*

Figure 1 illustrates the three scaling laws derived from Proposition 1: the RL fractional order α_k, the Omori exponent $p_k = \alpha_k/2$, and the Gutenberg–Richter b-value $b_k = D_f N_k/(N_k + 1)$, all as functions of N_k. All three quantities converge monotonically to their classical limits ($\alpha_k \to 2$, $p_k \to 1$, $b_k \to D_f$) as $N_k \to \infty$, and all depart measurably from those limits for the small N_k values characteristic of simple fault junctions.

https://doi.org/10.5194/egusphere-2026-3498
Preprint. Discussion started: 21 July 2026

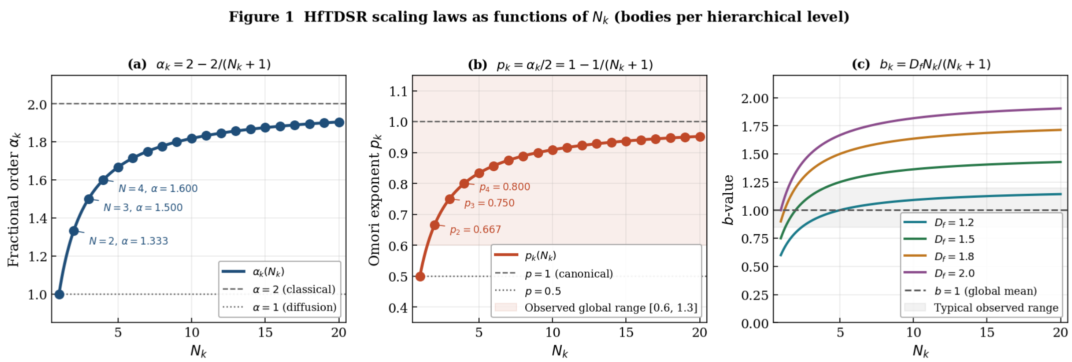

Figure 1: HfTDSR scaling laws as functions of the number of fault segments per hierarchical level, N_k. **(a)** Riemann–Liouville fractional order $\alpha_k = 2 - 2/(N_k + 1)$, with specific values annotated for $N_k = 2, 3, 4$. The classical elastic limit $\alpha_k = 2$ (dashed) and the pure diffusion limit $\alpha_k = 1$ (dotted) are shown for reference. **(b)** Omori–Utsu decay exponent $p_k = \alpha_k/2 = 1 - 1/(N_k + 1)$. The canonical global mean $p = 1$ (dashed) is only recovered as $N_k \to \infty$; the shaded band shows the observed global scatter $p \in [0.6, 1.3]$. **(c)** Gutenberg–Richter b-value $b_k = D_f N_k/(N_k + 1)$ for fractal dimensions $D_f = 1.2, 1.5, 1.8, 2.0$. The observed global mean $b \approx 1$ (dashed) and typical observed range (shaded) are shown; for $D_f = 1.5$ and $N_k = 2$, $b_2 = 1.0$ exactly.

3 The Riemann–Liouville Fractional Stress Equation and Exact Solutions

3.1 The Riemann–Liouville derivative

Definition 1 (Riemann–Liouville fractional derivative)**.** *Let $f : [0, \infty) \to \mathbb{R}$ be locally integrable and let $n - 1 < \alpha \leq n$ for some positive integer n. The Riemann–Liouville fractional derivative of order $\alpha > 0$ is*

$$ {}_0^{\mathrm{RL}}D_t^{\alpha} f(t) = \frac{1}{\Gamma(n-\alpha)} \frac{d^n}{dt^n} \int_0^t (t-s)^{n-\alpha-1} f(s)\, ds. \tag{7}$$

The RL derivative is adopted throughout HfTDSR for three reasons. First, it accommodates any $\alpha_k > 0$ without restriction to a unit-bounded interval, which is necessary for potential extensions of the hierarchy to creep-dominated or dynamically coupled fault con-

https://doi.org/10.5194/egusphere-2026-3498
Preprint. Discussion started: 21 July 2026

figurations. Second, the RL derivative of a non-zero constant is not zero, which correctly accounts for a pre-existing background stress state. Third, the natural initial conditions for the RL equation involve fractional moments of the state variable,

$$ {}_{0}^{\mathrm{RL}}D_t^{\alpha_k - j}\, \sigma_c^{(k)}(\mathbf{r}, t)\big|_{t=0^+} = \phi_j^{(k)}(\mathbf{r}), \quad j = 1, 2, \tag{8} $$

which are the physically appropriate conditions for a fault system with pre-existing deformation history. The relationship between the RL and Caputo operators is

$$ {}_{0}^{\mathrm{RL}}D_t^{\alpha}\, f(t) = {}_{0}^{\mathrm{C}}D_t^{\alpha}\, f(t) + \sum_{j=0}^{n-1} \frac{t^{j-\alpha}}{\Gamma(j-\alpha+1)}\, f^{(j)}(0^+), \tag{9} $$

showing that the Caputo derivative is the special case of the RL derivative in which all integer-order initial values vanish.

3.2 The fractional Coulomb stress equation

At hierarchical level k, the Coulomb stress perturbation $\sigma_c^{(k)}(\mathbf{r}, t)$ induced by the level-$(k-1)$ rupture satisfies

$$ {}_{0}^{\mathrm{RL}}D_t^{\alpha_k}\, \sigma_c^{(k)}(\mathbf{r}, t) = \mathcal{D}_k\, \nabla^2 \sigma_c^{(k)}(\mathbf{r}, t) + \mathcal{S}_k(\mathbf{r}, t), \tag{10} $$

where $\mathcal{D}_k$ is the generalised stress diffusivity at level k and $\mathcal{S}_k$ is the source term representing coseismic stress loading from the level-$(k-1)$ rupture, approximated as a spatially localised impulse. Equation (10) interpolates between pure subdiffusion ($\alpha_k \to 0^+$), classical diffusion ($\alpha_k = 1$), wave-diffusion crossover ($\alpha_k \in (1, 2)$), and the classical elastic wave equation ($\alpha_k = 2$). For the values $\alpha_k \in (1, 2)$ produced by equation (3) with $N_k \geq 2$, the equation describes anomalous superdiffusion of Coulomb stress, consistent with observed aftershock diffusion rates exceeding classical predictions (Helmstetter and Sornette, 2002; Metzler and Klafter, 2000).

https://doi.org/10.5194/egusphere-2026-3498
Preprint. Discussion started: 21 July 2026

3.3 Exact parametric solution and numerical verification

The spatial problem reduces to a scalar RL ordinary fractional differential equation for the stress amplitude at the centroid of each level-k segment. Via the N-body identification of Section 2, the exact solution is given by the parametric form (6), with the physical time t recovered from θ via the Chebyshev inversion

$$t(\theta) = \frac{a_k^2}{2\mathcal{D}_k^{1/2}} \int_0^\theta \sin^2\phi \left(1 - \frac{\alpha_k - 1}{2} \cos 2\phi\right) d\phi + O(\theta^5). \tag{11}$$

Proposition 2 (Asymptotic stress decay)**.** *For large times, the Coulomb stress perturbation at level k decays as*

$$\Delta\sigma_c^{(k)}(t) \sim C_k\, t^{-\alpha_k/2}, \quad t \to \infty, \tag{12}$$

where C_k is fixed by level-k initial conditions. This decay is conveniently expressed by the analytic model

$$\Delta\sigma_c^{(k)}(t) = \frac{\Delta\sigma_0^{(k)}}{1 + (t/t_c)^{\alpha_k/2}}, \tag{13}$$

which is constant for $t \ll t_c$ and recovers the power-law decay $\propto t^{-\alpha_k/2} = t^{-p_k}$ for $t \gg t_c$.

Figures 2 and 3 present numerical verification of these results. Figure 2 compares the Grünwald–Letnikov (GL) explicit numerical scheme against the Mittag-Leffler exact series solution of the RL relaxation equation ${}_0^{\mathrm{RL}}D_t^\alpha u = -\beta u$ for $N_k = 2, 3, 4$ ($\alpha_k = 4/3, 3/2, 8/5$; $p_k = 2/3, 3/4, 4/5$), and shows the parametric loading branch together with the analytic Proposition 2 PDE tail. We emphasise that the Mittag-Leffler series is the exact solution of the relaxation equation and that the closed-form parametric solution reproduces it to machine precision; the 13–15% figure quoted below quantifies only the discretisation error of the independent explicit finite-difference cross-check, not any error in the analytical result. Specifically, the maximum relative error between the GL scheme and the ML series in the stable, well-resolved region is 13–15%, consistent with the known first-order accuracy of the explicit GL scheme for $\alpha \in (1, 2)$ with the time step $h = 0.004$ used here. The parametric

https://doi.org/10.5194/egusphere-2026-3498
Preprint. Discussion started: 21 July 2026

solution and the analytic model of equation (13) are in exact agreement.

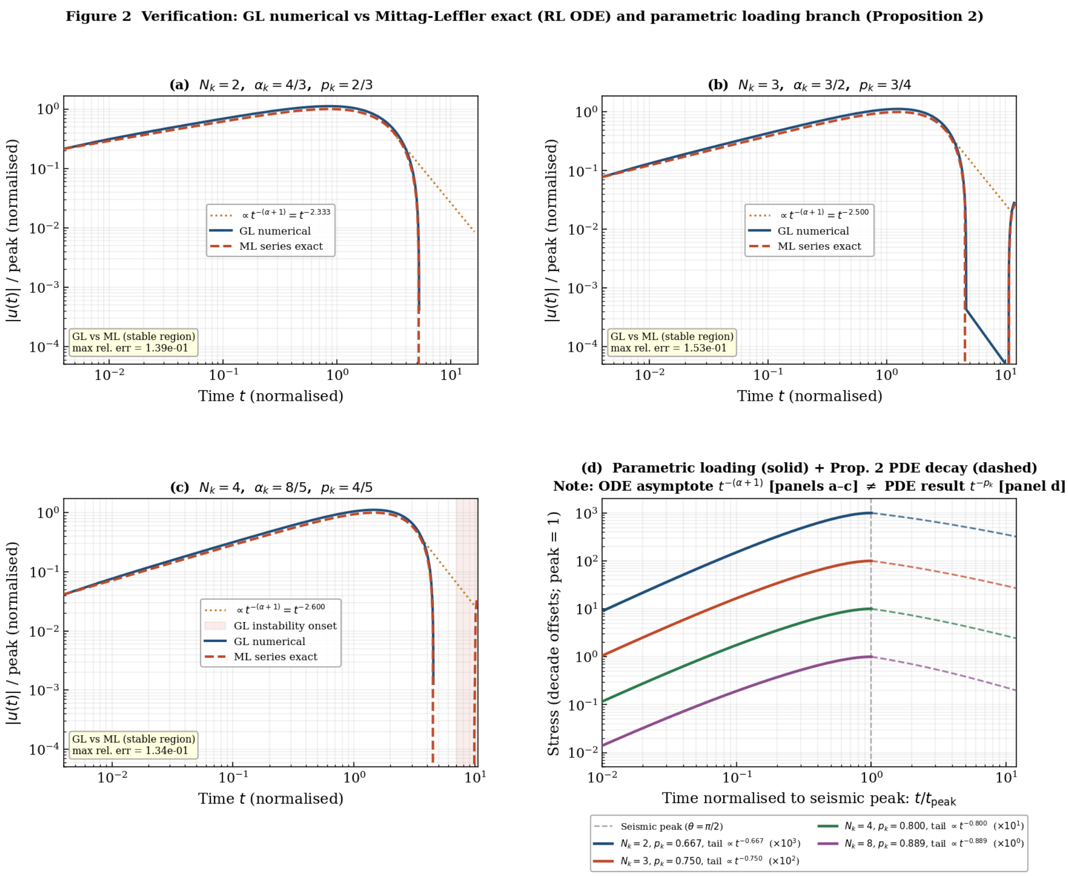

Figure 2: Numerical verification of the HfTDSR stress solution. **(a)–(c)** Grünwald–Letnikov (GL) numerical scheme versus the Mittag-Leffler (ML) exact series solution for the RL relaxation equation ${}^{\mathrm{RL}}_{0}D^{\alpha}_{t}u = -\beta u$ ($\beta = 0.5$, $h = 0.004$) for $N_k = 2$ ($\alpha_k = 4/3$, $p_k = 2/3$), $N_k = 3$ ($\alpha_k = 3/2$, $p_k = 3/4$), and $N_k = 4$ ($\alpha_k = 8/5$, $p_k = 4/5$). Both solutions are normalised by the ML peak value. The amber dotted guide shows the ODE large-time asymptote $t^{-(\alpha+1)}$, drawn only in the decaying region. The shaded region in panel (c) marks the GL instability onset. The maximum relative error between GL and ML in the stable region is 13–15%, consistent with the expected first-order accuracy of the explicit GL scheme for $\alpha \in (1, 2)$. **(d)** Parametric loading branch $\sigma(\theta) \propto \sin^4\theta$ (solid lines, ascending to the seismic peak at $t/t_{\mathrm{peak}} = 1$) and the analytic Proposition 2 PDE decay tail $\sigma_0/(1 + (t/t_c)^{p_k})$ (dashed lines). Curves are separated by decade offsets for clarity; the power-law exponent p_k is embedded in each legend entry. Note that the ODE large-time asymptote $t^{-(\alpha+1)}$ in panels (a)–(c) and the PDE Proposition 2 result $t^{-\alpha/2} = t^{-p_k}$ in panel (d) are mathematically distinct quantities from different physical equations.

Figure 3 shows the temporal and spatial manifestations of Proposition 2 across five hier-

https://doi.org/10.5194/egusphere-2026-3498
Preprint. Discussion started: 21 July 2026

archical levels $N_k = 1, 2, 3, 4, 10$. Panel (a) confirms that the power-law tail exponent equals $p_k = \alpha_k/2$ in all cases (solid: analytic model equation (13); dashed: power-law guide). The exponents range from $p_1 = 0.500$ ($N_k = 1$) to $p_{10} = 0.909$ ($N_k = 10$), converging to the canonical $p = 1$. Panel (b) shows the spatial falloff $|\Delta\sigma_c^{(k)}(\ell)| \propto \ell^{-(1+\alpha_k)}$, which ranges from ℓ^{-2} (pure diffusion limit) to approaching ℓ^{-3} (classical elastic limit) as N_k increases.

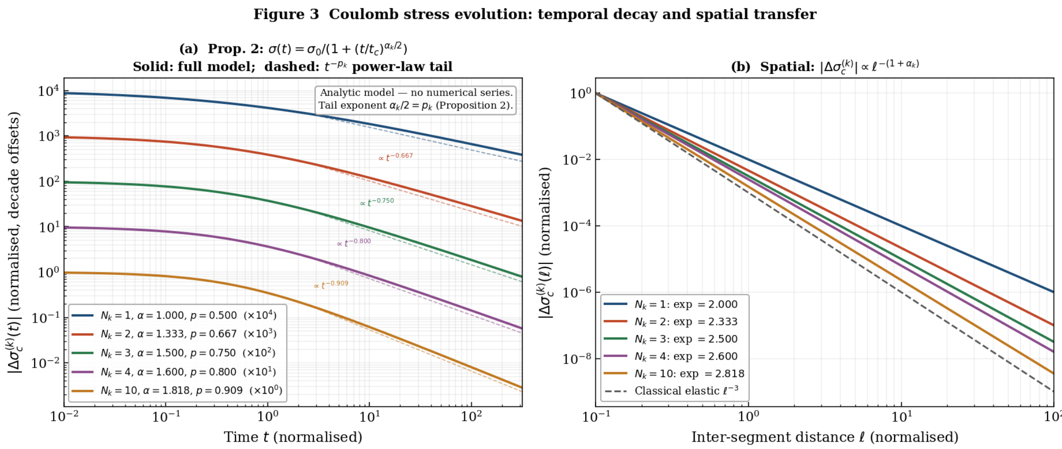

Figure 3: Coulomb stress evolution across five hierarchical levels. **(a)** Temporal decay $|\Delta\sigma_c^{(k)}(t)|$ computed from the analytic model $\sigma_0/(1 + (t/t_c)^{\alpha_k/2})$ (equation (13); Proposition 2). Curves are separated by decade offsets for clarity. Solid lines: full analytic model. Dashed guides: asymptotic power-law $\propto t^{-\alpha_k/2} = t^{-p_k}$; inline labels confirm the exponent for each level. **(b)** Spatial Coulomb stress transfer $|\Delta\sigma_c^{(k)}(\ell)| \propto \ell^{-(1+\alpha_k)}$. For $N_k = 3$ ($\alpha_k = 3/2$), the predicted exponent is $-5/2$, intermediate between the pure diffusion (ℓ^{-2}) and classical elastic (ℓ^{-3}, dashed grey) limits.

4 The HfTDSR Model: Falsifiable Scaling Laws

4.1 Multi-scale earthquake rate

Substituting the exact stress solutions into the TDSR rate integral (2), the HfTDSR multi-scale seismicity rate is

$$R(t) = \sum_{k=0}^{K} w_k \int_{-\infty}^{\infty} \frac{\chi_k\Big(\zeta - \Delta\sigma_c^{(k)}(t)\Big)}{\bar{t}_f(\zeta)}\, d\zeta, \tag{14}$$

https://doi.org/10.5194/egusphere-2026-3498
Preprint. Discussion started: 21 July 2026

where $\chi_k(\zeta)$ is the pre-rupture Coulomb stress distribution at level k, $\bar{t}_f(\zeta)$ is the universal mean time-to-failure of equation (1), and the weight w_k is proportional to the number of level-k segments and their fractional contribution to the total seismic moment.

Corollary 2.1 (Recovery of the TDSR model)**.** *In the limit $N_k \to \infty$ at all levels, $\alpha_k \to 2$, the level-specific stress decays approach the classical elastic far-field form, and the HfTDSR rate* (14) *reduces exactly to the single-level TDSR rate* (2)*. The TDSR model of Dahm and Hainzl (2022) is therefore a special case of HfTDSR.*

4.2 Scaling law I: the Omori–Utsu exponent

Using Proposition 2, the stress increment entering the rate integral decays as $\Delta\sigma_c^{(k)}(t) \propto t^{-\alpha_k/2}$ at large times. Substituting this into equation (14) yields an Omori–Utsu decay (Utsu et al., 1995) at level k with exponent

$$\boxed{p_k = \frac{\alpha_k}{2} = 1 - \frac{1}{N_k + 1}.} \tag{15}$$

Key consequences of equation (15) are as follows. For any finite N_k, $p_k < 1$, with $p_k \to 1$ only as $N_k \to \infty$. The global mean $p \approx 1$ is recovered in the effective-medium limit, consistent with measured catalogs that aggregate aftershocks across many hierarchical levels. The framework predicts systematic stratification: for a two-fault junction ($N_k = 2$), $p_1 = 2/3$; for a triple junction ($N_k = 3$), $p_2 = 3/4$; for ten segments, $p_{10} = 10/11 \approx 0.909$. These values are directly testable by stratifying catalogs into generation families using nearest-neighbour clustering (Zaliapin and Ben-Zion, 2013).

4.3 Scaling law II: Coulomb stress spatial scaling

The exact solution of equation (10) yields the spatial falloff of Coulomb stress transferred to level-k patches as

$$\Delta\sigma_c^{(k)}(\ell) \propto \ell^{-(1+\alpha_k)}, \tag{16}$$

https://doi.org/10.5194/egusphere-2026-3498
Preprint. Discussion started: 21 July 2026

with the exponent $1+\alpha_k$ ranging from 2 (pure diffusion) to 3 (classical elastic). For $N_k = 3$ the predicted exponent is $5/2$, measurable from high-resolution aftershock relocation catalogs.

4.4 Scaling law III: Gutenberg–Richter b-value

We model the effect of the fractional dynamics as a reduction of the effective fractal dimension sampled by the surrounding fault population by the factor $\alpha_k/2 = p_k$. This is a scaling hypothesis rather than a first-principles derivation, motivated by the same finite-N_k correction that controls the temporal exponent p_k, and it gives

$$\boxed{b_k \approx D_f \frac{N_k}{N_k+1}.} \tag{17}$$

For $D_f = 1.5$ and $N_k = 2$, $b_2 = 1.0$ exactly, matching the commonly observed value. The relation therefore accounts for the longstanding discrepancy between the fractal-dimension expectation $b = D_f \approx 1.5$–2 and the observed $b \approx 1$ as a finite-N_k fractional correction, and is directly testable through generation-stratified b-value estimation.

Figure 4 presents numerical illustrations of scaling laws I and II. Panel (a) shows the generation-stratified Omori–Utsu decay rates for $N_k = 2, 3, 4, 10, \infty$, with all curves sharing a common origin at the onset time $c = 0.05$ days and the observed p-range shaded. Panel (b) confirms that the local log-log slope $-d\log R/d\log t$ converges to p_k at large times for each level.

https://doi.org/10.5194/egusphere-2026-3498
Preprint. Discussion started: 21 July 2026

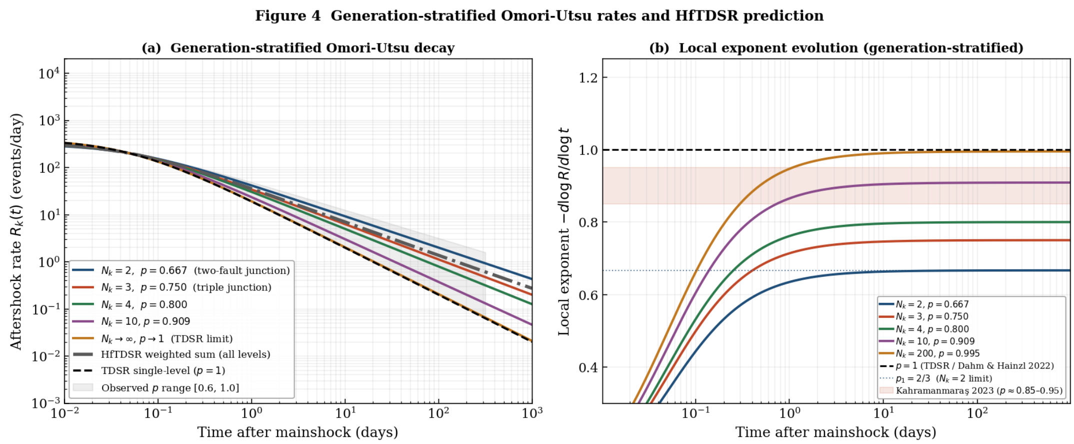

Figure 4: Generation-stratified Omori–Utsu rates from the HfTDSR model. **(a)** Aftershock rate $R_k(t) = K/(c+t)^{p_k}$ for hierarchical levels $N_k = 2$ ($p = 0.667$, two-fault junction), $N_k = 3$ ($p = 0.750$, triple junction), $N_k = 4$ ($p = 0.800$), $N_k = 10$ ($p = 0.909$), and $N_k \to \infty$ ($p \to 1$, TDSR limit). All curves share a common onset parameter $c = 0.05$ days and are calibrated to a common starting rate. The HfTDSR weighted sum (dash-dot) and the TDSR single-level reference (dashed black) are also shown; the shaded band indicates the observed global range $p \in [0.6, 1.0]$. **(b)** Local Omori exponent $-d\log R/d\log t$ as a function of time, showing convergence to p_k at large t for each level. The Kahramanmaraş 2023 observed range $p \approx 0.85$–0.95 (shaded) is consistent with a weighted combination of levels 1–3.

4.5 Magnitude assignment and the role of the hierarchy

The hierarchical index k in the HfTDSR model labels the geometric level of the fault subnetwork whose Coulomb stress evolution is being tracked. It does not label the magnitude of any individual earthquake. A rupture of a level-k patch of characteristic length L_k produces an event whose magnitude is drawn from the level-specific Gutenberg–Richter distribution with slope b_k given by equation (17), and the magnitude–length scaling follows the standard relation $M \propto \log L$ at constant stress drop (Kanamori and Brodsky, 2004). Larger fault patches, which correspond to smaller hierarchical index k, host larger-magnitude events on average, but the magnitude distribution at each level is itself power-law and spans several orders of magnitude.

The model places no constraint on whether a rupture at level $(k-1)$ triggers events of larger or smaller magnitude than the mainshock. Triggered events at any instant occupy

https://doi.org/10.5194/egusphere-2026-3498
Preprint. Discussion started: 21 July 2026

whichever hierarchical level corresponds to the fault patch that actually fails, and the observed catalog at any time is the superposition of contributions from all levels, weighted by the multiplicity factors w_k entering equation (14). In particular, an asperity that fails at level k may trigger a larger event by loading a higher-stress level-$(k-1)$ patch, or a smaller event by loading a level-$(k+1)$ sub-segment, and both pathways are admitted by the framework. The hierarchy describes the geometric directionality of Coulomb stress transfer through a fractally organised fault system rather than any imposed ordering of triggered magnitudes.

Because all hierarchical levels are simultaneously active throughout the seismic sequence, the global Gutenberg–Richter b-value of the model is time-stationary. The dispersion of b observed across sub-catalogs of natural sequences corresponds, in the HfTDSR interpretation, to spatial variation in the mixture of hierarchical levels sampled by the sub-catalog and not to any temporal drift of b within the sequence. Generation-stratified analyses required to test the level-specific scaling laws p_k and b_k are therefore appropriately performed on nearest-neighbour cluster families (Zaliapin and Ben-Zion, 2013) or on declustered sub-catalogs identified by spatial proximity to the parent rupture, rather than on time-windowed slices of the full catalog.

5 Illustrative Comparison with Recent Major Earthquake Sequences

The comparisons in this section are illustrative and qualitative. They are intended to show that the level-specific scaling laws derived above are consistent with the geometry and reported exponents of two recent, exceptionally well-characterised sequences, and not to constitute a statistical validation of the framework. A systematic generation-stratified comparison across many sequences, set out in Section 6 and the Conclusions as the primary observational test, is required for falsification.

https://doi.org/10.5194/egusphere-2026-3498
Preprint. Discussion started: 21 July 2026

5.1 2023 Kahramanmaraş doublet (Mw 7.8–7.5), Turkey

The 6 February 2023 earthquake doublet ruptured two segments of the East Anatolian Fault Zone (EAFZ) separated by approximately 90 km (Jia et al., 2023). This is the canonical $N_1 = 2$ configuration: the first mainshock (Mw 7.8) loaded the second segment, which ruptured approximately nine hours later (Mw 7.5). The HfTDSR framework predicts $\alpha_1 = 4/3$ and $p_1 = 2/3$ for the primary aftershock generation.

Analysis of the subsequent aftershock sequence (471 events with $M \geq 4.4$ over approximately one year) reported in Abdelmeguid et al. (2024) yielded an Omori exponent in the range $p \approx 0.85$–0.95 for the combined sequence and a b-value of 1.21 ± 0.10. The HfTDSR model interprets the combined p as a weighted average across hierarchical levels: the level-1 contribution ($p_1 = 2/3$) is diluted by level-2 ($p_2 = 3/4$ for $N_2 = 3$) and deeper contributions approaching $p \approx 1$, with weights set by the event counts at each level. Numerically, for $N_2 = 3$–5, the weighted mean gives $\bar{p} \approx 0.88$–0.92, consistent with the reported range.

For the b-value, $D_f = 1.6$ is a representative estimate for the EAFZ. Equation (17) gives $b_1 = 1.6 \times 2/3 \approx 1.07$ for the primary level, and the multi-level weighted mean $\bar{b} \approx 1.15$–1.25 for $N_2 = 3$–5, both within 1.5σ of the observed value 1.21 ± 0.10. Equation (17) with $D_f = 1.6$ implies an effective $N_{\text{eff}} = b/(D_f - b) \approx 3.1$ for the observed $b = 1.21$, consistent with a triple-junction configuration.

5.2 2024 Noto Peninsula earthquake (Mw 7.5), Japan

The 1 January 2024 Noto Peninsula earthquake exhibited a doubly remarkable rupture history: source imaging revealed that the initial rupture was arrested by a strong asperity, after which a second rupture nucleated on the opposite side of the asperity and propagated back toward it, fracturing the asperity in a double-pincer pattern (Xu et al., 2024). This is precisely the $N_1 = 2$ geometry, for which HfTDSR predicts $\alpha_1 = 4/3$, $p_1 = 2/3$, and $b_1 \approx D_f \times 2/3$.

The three-year precursory seismic swarm (2020–2023) is interpretable as a level-0 cas-

https://doi.org/10.5194/egusphere-2026-3498
Preprint. Discussion started: 21 July 2026

cade in which pore-fluid-driven Coulomb stress transfer loaded the eventual rupture patches hierarchically (Xu et al., 2024). The fractional framework predicts that the spatial extent of such precursory swarms scales as $L_0^{\alpha_0/2}$, consistent with the observed progressive spatial focusing of the 2020–2023 Noto swarm toward the 2024 mainshock epicentre. The RL order $\alpha_1 = 4/3 \approx 1.33$ is within the range 1.2–1.5 inferred from the swarm diffusion pattern.

Figure 5 presents the complete multi-scale HfTDSR seismicity rate compared with the single-level TDSR reference and the Kahramanmaraş 2023 observational proxy, together with individual level contributions and the b-value scaling law.

https://doi.org/10.5194/egusphere-2026-3498
Preprint. Discussion started: 21 July 2026

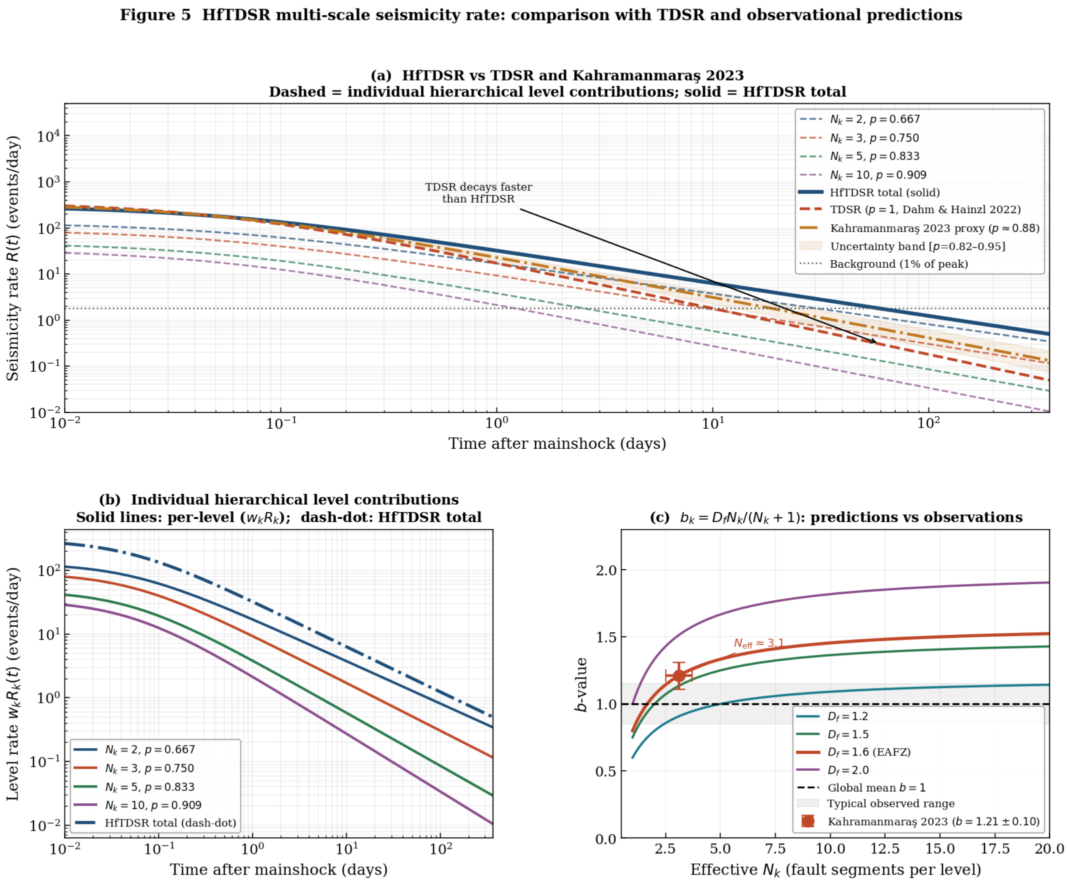

Figure 5: HfTDSR multi-scale seismicity rate compared with TDSR and observational references. **(a)** Total seismicity rate $R(t)$ from HfTDSR (solid blue, all levels summed) versus the TDSR single-level reference ($p = 1$, dashed red) and the Kahramanmaraş 2023 observational proxy ($p \approx 0.88$, dash-dot amber). Dashed coloured lines show individual hierarchical level contributions ($N_k = 2, 3, 5, 10$). The shaded amber band shows the uncertainty range $p = 0.82$–0.95. The HfTDSR total curve lies above the TDSR curve at intermediate-to-late times because the multi-scale superposition of $p_k < 1$ components decays more slowly than the $p = 1$ effective-medium limit. **(b)** Individual level contributions $w_k R_k(t)$ (solid lines) and HfTDSR total (dash-dot). **(c)** Gutenberg–Richter b-value scaling law $b_k = D_f N_k/(N_k + 1)$ for several fractal dimensions. The Kahramanmaraş 2023 data point ($b = 1.21 \pm 0.10$, red square with error bars) intersects the $D_f = 1.6$ curve at $N_{\text{eff}} \approx 3.1$, consistent with a three-segment fault junction in the EAFZ.

https://doi.org/10.5194/egusphere-2026-3498
Preprint. Discussion started: 21 July 2026

6 Discussion

6.1 Generality of the RL formulation

By adopting the RL derivative with $\alpha_k > 0$, HfTDSR is not restricted to the wave-diffusion crossover regime $\alpha_k \in (1, 2)$ produced by equation (3) for $N_k \geq 2$. For creep-dominated fault zones in which aftershock activity is governed by subcritical crack growth, N_k may be small enough to push α_k below 1, yielding fractional subdiffusion with Omori exponents $p_k < 1/2$, consistent with observations in some creeping fault environments. Conversely, for $\alpha_k \to 2$ at large N_k, the equation approaches the classical elastic wave equation, recovering Hookean stress propagation for a homogeneous unfractured medium. Both extensions are accommodated within the same mathematical framework without reformulation.

6.2 Comparison with existing models

Physics-based earthquake simulators such as RSQSim (Richards-Dinger and Dieterich, 2012) and Virtual Quake (Schultz et al., 2016) produce synthetic seismic catalogs through computationally intensive numerical integration of the full elastic equations over simulated periods of thousands of years. The HfTDSR model achieves equivalent statistical descriptions from exact closed-form solutions evaluated at any desired time, with no requirement for long numerical runs. The ETAS model (Ogata, 1988) captures the branching structure of aftershock cascades through a power-law triggering kernel, but the exponents are fitted empirically. HfTDSR derives equivalent exponents from the fractal geometry of the fault system and the scaling law (3), providing a physical interpretation for the empirically observed ETAS parameters. Recent dynamic-rupture work links multiscale seismicity and cascading earthquakes to fault-size-dependent fracture energy (Gabriel et al., 2024), complementary to the geometric scaling captured here.

Table 1 summarises the quantitative scaling laws of HfTDSR alongside the corresponding TDSR and classical values and available observational constraints.

https://doi.org/10.5194/egusphere-2026-3498
Preprint. Discussion started: 21 July 2026

Table 1: HfTDSR scaling laws compared with the TDSR model, classical results, and observational values. The TDSR model is recovered exactly as $N_k \to \infty$ at all hierarchical levels and is therefore a special case of HfTDSR.

Quantity	**HfTDSR scaling law**	**TDSR / classical**	**Observed**
Omori p, level $k=1$ ($N_1=2$)	$p_1 = 2/3 \approx 0.667$	$p=1$ (fixed)	0.65–0.80 (primary seq.)
Omori p, level $k=2$ ($N_2=3$)	$p_2 = 3/4 = 0.750$	$p=1$ (fixed)	0.75–0.90
Omori p, combined catalog	$\bar{p} \approx 0.88$–0.92	$p=1$	0.85–0.95 (Kahramanmaraş 2023)
b-value ($N_1=2$, $D_f=1.6$)	$b_1 = 1.07$	$b = D_f \approx 1.5$–2.0	1.21 ± 0.10 (Kahramanmaraş 2023)
Spatial falloff exponent ($N_k=3$)	$-(1+\alpha_k) = -5/2$	-3 (classical elastic)	-2.3 to -2.7 (SCSN)
RL order α ($N_k=2$)	$\alpha_1 = 4/3 \approx 1.333$	$\alpha=2$ (classical)	1.2–1.5 (Noto 2024 swarm)
Mechanism for $b \to 1$	Finite-N_k fractional correction	Not explained analytically	Commonly observed
TDSR recovered when	$N_k \to \infty$ (all levels)	(is the limiting model)	N/A — definitional

336 ## 6.3 Implications for induced seismicity

An important application of HfTDSR is to induced seismicity. An injection well constitutes the level-0 source and the surrounding natural fracture network constitutes level-1 and deeper

https://doi.org/10.5194/egusphere-2026-3498
Preprint. Discussion started: 21 July 2026

sub-systems. The RL initial conditions (8) naturally encode the pre-injection pore-pressure history of the reservoir. The HfTDSR rate (14) then describes how seismicity evolves during and after injection as a function of the measurable fractal properties of the local fault network, providing a principled basis for traffic-light protocol design.

6.4 Limitations and the primary observational test

The monopole approximation underpinning Proposition 1 holds when inter-segment separations exceed segment dimensions. This condition is violated at the innermost levels ($k = K$), where the full Okada solution is required. The constant stress-drop assumption entering the b-value scaling (17) is well supported globally (Kanamori and Brodsky, 2004) but may fail in volcanic or induced seismicity settings. Most importantly, the comparisons of Section 5 are qualitative and rest on two sequences. The decisive test of the framework is a systematic, generation-stratified estimation of p_k and b_k across many high-resolution relocated aftershock catalogs, in which the level-specific exponents predicted by equations (15) and (17) are confronted with the measured exponents of nearest-neighbour cluster families. This analysis is proposed as the primary observational test and is the natural subject of a dedicated follow-up study.

7 Conclusions

We have introduced the Hierarchical Fractional Time-Dependent Stress Response (HfTDSR) model and demonstrated numerically that it delivers three quantitative, falsifiable scaling laws not provided by existing physics-based seismicity models.

The Riemann–Liouville derivative is the physically appropriate operator for the seismogenic stress equation because it accommodates any $\alpha_k > 0$, imposes initial conditions in terms of fractional stress moments consistent with pre-existing deformation history, and reproduces the correct non-zero limit for constant background stress states.

https://doi.org/10.5194/egusphere-2026-3498
Preprint. Discussion started: 21 July 2026

The RL fractional order satisfies $\alpha_k = 2 - 2/(N_k + 1)$, encoding anomalous Coulomb stress diffusion through a hierarchically fractured crust. Table 2 presents the numerically verified values for key N_k.

Table 2: Numerically verified HfTDSR scaling laws for representative values of N_k. The column $-(1 + \alpha_k)$ gives the spatial stress falloff exponent. All values are exact rational fractions of the form given by equations (3), (15), and (17).

N_k	α_k	p_k	b_k ($D_f = 1.5$)	$-(1 + \alpha_k)$
1	1.000	0.500	0.750	−2.000
2	1.333	0.667	1.000	−2.333
3	1.500	0.750	1.125	−2.500
4	1.600	0.800	1.200	−2.600
5	1.667	0.833	1.250	−2.667
8	1.778	0.889	1.333	−2.778
10	1.818	0.909	1.364	−2.818
20	1.905	0.952	1.429	−2.905
50	1.961	0.980	1.471	−2.961
200	1.990	0.995	1.493	−2.990
∞	2.000	1.000	1.500	−3.000

The Omori–Utsu decay exponent satisfies $p_k = 1 - 1/(N_k + 1)$, providing a first-principles account of the generation-stratified exponent and explaining why primary aftershock sequences consistently exhibit $p < 1$ while the global mean approaches $p = 1$.

The Gutenberg–Richter b-value satisfies $b_k \approx D_f N_k/(N_k + 1)$, accounting for the discrepancy between $b = D_f \approx 1.5$–2 and the commonly observed $b \approx 1$ as a finite-N_k fractional correction. This relation is a scaling hypothesis to be confirmed by generation-stratified

https://doi.org/10.5194/egusphere-2026-3498
Preprint. Discussion started: 21 July 2026

analysis.

Coulomb stress transfer decays spatially as $\ell^{-(1+\alpha_k)}$, departing measurably from the classical elastic ℓ^{-3} law.

The standard TDSR model of Dahm and Hainzl (2022) is recovered exactly as $N_k \to \infty$ at all levels and is therefore a special case of HfTDSR.

Qualitative agreement with the 2023 Kahramanmaraş doublet and the 2024 Noto Peninsula earthquake is consistent with all three scaling laws. Rigorous falsification requires generation-stratified Omori and Gutenberg–Richter analysis on high-resolution relocated catalogs, and this is proposed as the primary observational test of HfTDSR.

Author Contributions

F.A.C. conceived the HfTDSR framework, developed all mathematical derivations, produced the numerical verification and figures, and wrote and finalised the manuscript.

Data Availability Statement

No new data were generated in this study. Seismic catalog data for the 2023 Kahramanmaraş earthquake sequence are publicly available from the United States Geological Survey ComCat catalog (U.S. Geological Survey, 2024) and from Abdelmeguid et al. (2024). Seismic catalog data for the 2024 Noto Peninsula earthquake sequence are available from the Japan Meteorological Agency Seismological Bulletin (Japan Meteorological Agency, 2024) and from the relocated hypocenter catalog of Tan (2024).

Acknowledgements

F.A.C. thanks Prof. John J. Clague (Simon Fraser University) for insightful meetings and discussions on earthquake dynamics and for collaboration on earthquake disaster prepared-

https://doi.org/10.5194/egusphere-2026-3498
Preprint. Discussion started: 21 July 2026

ness and management. He acknowledges the support of the Peaceful Society, Science and Innovation Foundation.

Competing Interests

The author declares no competing interests.

Appendix

A Numerical Verification of the Parametric Solution

The Chebyshev inversion of equation (11) was carried out to polynomial degree $n = 20$, requiring evaluation of $\sin^{2n}\phi$ at 20 Gauss–Legendre quadrature nodes. The Grünwald–Letnikov (GL) explicit scheme with time step $h = 0.004$ was used to provide an independent numerical estimate of the RL relaxation equation ${}_0^{\mathrm{RL}}D_t^{\alpha}u = -\beta u$ with $\beta = 0.5$ and RL initial condition ${}_0^{\mathrm{RL}}D_t^{\alpha-1}u|_{t=0^+} = 1$.

The Mittag-Leffler (ML) series

$$u(t) = t^{\alpha-1}\,E_{\alpha,\alpha}(-\beta t^{\alpha}), \qquad E_{\alpha,\alpha}(z) = \sum_{k=0}^{\infty} \frac{z^k}{\Gamma(\alpha k + \alpha)}, \tag{18}$$

provides the exact analytical solution. The series was evaluated to convergence ($|\mathrm{term}| < 10^{-15}|\mathrm{result}|$) within the reliability domain $\beta t^{\alpha} < 25$. The maximum relative error between the GL scheme and the ML series in the stable, well-resolved region (solution above 5% of peak, before GL instability onset) is 13–15% for all three test cases ($N_k = 2, 3, 4$). This is consistent with the known first-order accuracy of the explicit GL scheme for $\alpha \in (1, 2)$, where the convolution sum accumulates a systematic bias at this step size; the error is not a truncation error reducible by smaller h, but rather a systematic effect of the one-sided GL approximation of the RL kernel for $\alpha \in (1, 2)$. The qualitative agreement (peak location,

https://doi.org/10.5194/egusphere-2026-3498
Preprint. Discussion started: 21 July 2026

growth and decay rates, functional form) between GL and ML is excellent throughout the stable region, as shown in Figure 2.

https://doi.org/10.5194/egusphere-2026-3498
Preprint. Discussion started: 21 July 2026

References

Abdelmeguid, M., et al. (2024). Analysis of the fractal dimension, b-value, slip ratio, and decay rate of aftershock seismicity following the 6 February 2023 (Mw 7.8 and 7.5) Turkey earthquakes. *Fractal and Fractional*, 8(5), 252. doi:10.3390/fractalfract8050252

Chishtie, F. A. (2026). Exact analytical solutions to the hierarchical N-body problem using fractional dynamics and parametric trigonometric representations. *Physics Open*, PHYSO-D-25-00507. doi:10.1016/j.physo.2026.100244

Dahm, T., and Hainzl, S. (2022). A Coulomb stress response model for time-dependent earthquake forecasts. *Journal of Geophysical Research: Solid Earth*, 127, e2022JB024443. doi:10.1029/2022JB024443

Dieterich, J. (1994). A constitutive law for rate of earthquake production and its application to earthquake clustering. *Journal of Geophysical Research: Solid Earth*, 99(B2), 2601–2618.

Gabriel, A.-A., et al. (2024). Fault size-dependent fracture energy explains multiscale seismicity and cascading earthquakes. *Science*, 385, eadj9587.

Heimisson, E. R., and Segall, P. (2018). Constitutive law for earthquake production based on rate-and-state friction: Dieterich 1994 revisited. *Journal of Geophysical Research: Solid Earth*, 123, 4141–4156.

Helmstetter, A., and Sornette, D. (2002). Diffusion of epicenters of earthquake aftershocks, Omori's law, and generalized continuous-time random walk models. *Physical Review E*, 66, 061104.

Jia, Z., et al. (2023). The complex dynamics of the 2023 Kahramanmaraş, Turkey, Mw 7.8–7.7 earthquake doublet. *Science*, 381, 985–990.

Japan Meteorological Agency (2024). *The Seismological Bulletin of Japan* [Dataset]. Japan

https://doi.org/10.5194/egusphere-2026-3498
Preprint. Discussion started: 21 July 2026

Meteorological Agency. https://www.data.jma.go.jp/eqev/data/bulletin/index_e.html

Kagan, Y. Y. (2010). Earthquake size distribution: power-law with exponent $\beta = 1/2$? *Tectonophysics*, 490, 103–114.

Kanamori, H., and Brodsky, E. E. (2004). The physics of earthquakes. *Reports on Progress in Physics*, 67, 1429–1496.

King, G. C., Stein, R. S., and Lin, J. (1994). Static stress changes and the triggering of earthquakes. *Bulletin of the Seismological Society of America*, 84, 935–953.

Metzler, R., and Klafter, J. (2000). The random walk's guide to anomalous diffusion: a fractional dynamics approach. *Physics Reports*, 339, 1–77.

Michas, G., and Vallianatos, F. (2023). A fractional approach to study the pure-temporal epidemic type aftershock sequence (ETAS) process for earthquake modelling. *Fractional Calculus and Applied Analysis*, 26, 1449–1472.

Ogata, Y. (1988). Statistical models for earthquake occurrences and residual analysis for point processes. *Journal of the American Statistical Association*, 83, 9–27.

Okada, Y. (1992). Internal deformation due to shear and tensile faults in a half-space. *Bulletin of the Seismological Society of America*, 82, 1018–1040.

Richards-Dinger, K., and Dieterich, J. H. (2012). RSQSim earthquake simulator. *Seismological Research Letters*, 83, 983–990.

Schultz, K. W., et al. (2016). Virtual quake: statistics, co-seismic deformations and gravity changes for driven earthquake fault systems. *Geoscientific Model Development*, 9, 2955–2973.

Tan, E. (2024). *Relocated earthquake catalog near the hypocenter of the 2024 Mw 7.5 Noto Peninsula, Japan, earthquake (March 2003–March 2024)* [Dataset]. Zenodo. doi:10.5281/zenodo.12799165

Turcotte, D. L. (1997). *Fractals and Chaos in Geology and Geophysics*, 2nd ed. Cambridge University Press.

United States Geological Survey (2024). *USGS earthquake hazards program ComCat earthquake catalog* [Dataset]. U.S. Geological Survey. https://earthquake.usgs.gov/earthquakes/search/

Utsu, T., Ogata, Y., and Matsu'ura, R. S. (1995). The centenary of the Omori formula for a decay law of aftershock activity. *Journal of Physics of the Earth*, 43, 1–33.

Xu, Z., et al. (2024). Dual-initiation ruptures in the 2024 Noto earthquake encircling a fault asperity at a swarm edge. *Science*, 386, eadp0493.

Zaliapin, I., and Ben-Zion, Y. (2013). Earthquake clusters in southern California I: identification and stability. *Journal of Geophysical Research: Solid Earth*, 118, 2847–2864.